HATS-11b AND HATS-12b: TWO TRANSITING HOT JUPITERS ORBITING SUB-SOLAR METALLICITY
STARS SELECTED FOR THE K2 CAMPAIGN 7[†]

M. Rabus[1,2], A. Jordán[1], J. D. Hartman[3], G. Á. Bakos[3], N. Espinoza[1], R. Brahm[1], K. Penev[3], S. Ciceri[2], G. Zhou[4], D. Bayliss[4,5], L. Mancini[2], W. Bhatti[3], M. de Val-Borro[3], Z. Csbury[3], B. Sato[6], T.-G. Tan[7], T. Henning[2], B. Schmidt[4], J. Bento[4], V. Suc[1], R. Noyes[8], J. Lázár[9], I. Papp[9], and P. Sári[9]

Draft version December 29, 2017

ABSTRACT

We report the discovery of two transiting extrasolar planets from the HATSouth survey. HATS-11, a V=14.1 G0-star shows a periodic 12.9 mmag dip in its light curve every 3.6192 days and a radial velocity variation consistent with a Keplerian orbit. HATS-11 has a mass of $1.000 \pm 0.060 \, M_\odot$, a radius of $1.444 \pm 0.057 \, R_\odot$ and an effective temperature of $6060 \pm 150 \, \mathrm{K}$, while its companion is a $0.85 \pm 0.12 \, M_\mathrm{J}$, $1.510 \pm 0.078 \, R_\mathrm{J}$ planet in a circular orbit. HATS-12 shows a periodic 5.1 mmag flux decrease every 3.1428 days and Keplerian RV variations around a V=12.8 F-star. HATS-12 has a mass of $1.489 \pm 0.071 \, M_\odot$, a radius of $2.21 \pm 0.21 \, R_\odot$ and an effective temperature of $6408 \pm 75 \, \mathrm{K}$. For HATS-12b, our measurements indicate that this is a $2.38 \pm 0.11 \, M_\mathrm{J}$, $1.35 \pm 0.17 \, R_\mathrm{J}$ planet in a circular orbit. Both host stars show sub-solar metallicity of -0.390 ± 0.060 dex and -0.100 ± 0.040 dex, respectively and are (slightly) evolved stars. In fact, HATS-11 is amongst the most metal-poor and, HATS-12 is amongst the most evolved stars hosting a hot Jupiter planet. Importantly, HATS-11 and HATS-12 have been observed in long cadence by Kepler as part of K2 campaign 7 (EPIC216414930 and EPIC218131080 respectively).

Subject headings: planetary systems — stars: individual (HATS-11, GSC 6308-00430, HATS-12, GSC 6304-00396) techniques: spectroscopic, photometric

1. INTRODUCTION

Transiting Extrasolar Planets, hereafter TEPs, allow us to measure many of their physical properties that are not accessible for non-transiting systems and thus occupy a prominent place among the nearly two thousands of exoplanets currently known.

One of the most important features of TEPs is that their radii can be measured from the transit shape if the radii of the stellar hosts are known. The radius, coupled with the measurement of the planetary mass from radial velocity (RV) observations, allows the computation of the bulk density of the planet and the possibility of inferring properties about its internal structure and composition.

The detection of close-in extrasolar giant planets has led to several theoretical challenges regarding their structure, formation, and subsequent evolution. One of the earliest realized challenges, and one which is yet to be solved, is the fact that close-in giant exoplanets often show radii that are far larger than those predicted by theories of giant planet evolution (e.g. HAT-P-32b Hartman et al. 2011). Moving forward in understanding the inflation mechanism will benefit from having larger samples of close-in, inflated gas giants, especially systems lying at some extreme of either planetary or stellar properties.

One of the most basic properties one can measure of a star is its metallicity, and much attention in the past has been given to the dependence of planet occurrence rate on the host star metallicity. Several studies have found that gas giants appear more frequently around metal-rich stars, both from RV programs (Santos et al. 2004; Valenti & Fischer 2005; Johnson et al. 2010) and from *Kepler* data (Schlaufman & Laughlin 2011; Buchhave et al. 2012; Everett et al. 2013; Wang & Fischer 2015). Discoveries of gas giants around metal-poor stars then add systems to a region of parameter space that is intrinsically less populated.

In this work we present two new inflated hot Jupiters orbiting metal poor stars discovered by the HATSouth survey: HATS-11b and HATS-12b. The structure of the paper is as follows. In Section 2 we summarize the detection of the photometric transit signal and the subsequent

[1] Instituto de Astrofísica, Facultad de Física, Pontificia Universidad Católica de Chile, Av. Vicuña Mackenna 4860, 7820436 Macul, Santiago, Chile; mrabus@astro.puc.cl
[2] Max Planck Institute for Astronomy, Heidelberg, Germany
[3] Department of Astrophysical Sciences, Princeton University, NJ 08544, USA
[4] Research School of Astronomy and Astrophysics, Australian National University, Canberra, ACT 2611, Australia
[5] Observatoire Astronomique de l'Université de Genève, 51ch. des Maillettes, 1290 Versoix, Switzerland
[6] Department of Earth and Planetary Sciences, Tokyo Institute of Technology, 2-12-1 Ookayama, Meguro-ku, Tokyo 152-8551, Japan
[7] Perth Exoplanet Survey Telescope, Perth, Australia
[8] Harvard-Smithsonian Center for Astrophysics, Cambridge, MA 02138, USA
[9] Hungarian Astronomical Association, Budapest, Hungary
[†] The HATSouth network is operated by a collaboration consisting of Princeton University (PU), the Max Planck Institute für Astronomie (MPIA), the Australian National University (ANU), and the Pontificia Universidad Católica de Chile (PUC). The station at Las Campanas Observatory (LCO) of the Carnegie Institute is operated by PU in conjunction with PUC, the station at the High Energy Spectroscopic Survey (H.E.S.S.) site is operated in conjunction with MPIA, and the station at Siding Spring Observatory (SSO) is operated jointly with ANU. Based in part on data collected at Subaru Telescope, which is operated by the National Astronomical Observatory of Japan. Based in part on observations made with the MPG 2.2 m Telescope at the ESO Observatory in La Silla.

spectroscopic and photometric observations of each star to confirm the planets. In Section 3 we analyze the data to rule out false positive scenarios and characterize the star and planet. In Section 4 we put our new systems in the context of the sample of the well characterized TEPs known to date.

2. OBSERVATIONS

2.1. *Photometric detection*

The initial images of HATS-11 and HATS-12 were obtained with the HATSouth wide-field telescope network consisting of 24 Takahashi E180 astrographs with an aperture of 18cm. The photons were detected with Apogee 4k × 4k U16M ALTA CCDs. Details on the time span and number of images are shown in Table 1. These images were processed following Penev et al. (2013). The light curves were trend-filtered following Kovács et al. (2005) and searched for periodic box-shaped signals using the Box Least-Squares (Kovács et al. 2002) method. For HATS-11 (2MASS 19173618-2223236; α = $19^{\mathrm{h}}17^{\mathrm{m}}36.24$s, δ = $-22°23'23.7''$; J2000; V=14.018 ± 0.081) the discovery light curve showed a photometric precision between 10 and 14 mmag per point and the BLS algorithm detected a dip of 12.9 mmag every 3.6192 days. For the brighter HATS-12 star (2MASS 19164857-1921212; α = $19^{\mathrm{h}}16^{\mathrm{m}}48.72$s, δ = $-19°21'21.2''$; J2000; V=12.756 ± 0.021) the precision was between 6 and 7 mmag per point and a periodic flux decrease of 5.1 mmag with P =3.1428 days was found, making this the third shallowest ground-based discovery to date (after HAT-P-11 (Bakos et al. 2010) and WASP-73 (Delrez et al. 2014)). Both light curves are shown in Figure 1 and the numerical data is available in Table 3. These initial detections triggered further spectroscopic and photometric follow-up observations in order to confirm the transit and the planetary nature as explained in the following sections.

2.2. *Spectroscopic Observations*

We started observing both candidates spectroscopically, in a process which is split into two kinds of spectroscopic observations. A first step of reconnaissance spectroscopy serves to reject possible astrophysical false positives, like e.g. binary stars, and to obtain a first estimate of stellar parameters. Afterwards, stable and high precision spectroscopic measurements allow us to obtain high precision radial velocity (RV) and line bisector (BS) time series for the stars. From this we can estimate the orbital parameters as well as the presence and mass of the companion for systems that are confirmed as planets, and a precise set of stellar parameters. The spectroscopic observations are summarized in Table 2.

HATS-11 was observed first with the ANU 2.3m telescope using the WiFES spectrograph and the duPont 2.5 m telescope using the echelle spectrograph. Details on the observing strategy and data reduction for the ANU 2.3m can be found in Bayliss et al. (2013) and for the duPont in Brahm et al. (2015). From these spectra we detect no RV variations greater than ~2 km s^{-1} and could determine the host star's spectral type. We verified with the new information that the transit is still consistent with a planetary companion. In light of this, we continued to observe HATS-11 with spectrographs al-

lowing for simultaneous wavelength calibration for RV precision, namely with CORALIE at the Euler 1.2m and FEROS at the MPG 2.2m telescope. For both spectrographs we made use of the reduction procedures described in Jordán et al. (2014) which gave us the RV and BS measurements of the spectrum. Similarly, HATS-12 was observed with the WiFES and the duPont echelle spectrograph. RVs/BSs were obtained with FEROS and additionally with the HDS spectrograph at the Subaru telescope. Details on the data reduction with HDS can be found in Sato et al. (2002, 2012). The phased high-precision RV and BS measurements are shown for each system in Figure 2; the data are presented in Table 6. Spectra, RVs and BSs are used in Section 3 to reject some possible systems mimicking a planetary system.

2.3. *Photometric follow-up observations*

We also photometrically followed-up both candidates with larger aperture telescopes. This is necessary because the HATSouth survey telescopes have limited photometric precision whereas the light curves obtained with these follow-up telescopes are of higher quality allowing us to better characterize the system. The distant in time photometric follow-up observations further help us to refine the transit ephemeris. Photometric follow-up observations are summarized in Table 1. The data are given in Table 3. The light curves for HATS-11 are shown in Figure 3 while for HATS-12 they are shown in Figure 4.

We obtained photometric time series of HATS-11 with the PEST 0.3 m, Swope 1 m, and the LCOGT 1 m networks. Data reduction followed the established procedures described in previous HATSouth discoveries (Penev et al. (2013); Mohler-Fischer et al. (2013); Bayliss et al. (2013); Jordán et al. (2014); Zhou et al. (2014b); Hartman et al. (2015); Brahm et al. (2015); Mancini et al. (2015)).

Additionally, a partial transit of HATS-11b was observed on 2014-09-07, in the K_s-band, using the IRIS2 infrared camera (Tinney et al. 2004) on the 3.9 m Anglo Australian Telescope, at Siding Spring Observatory, Australia. The instrument uses a Hawaii 1-RG detector, has a field of view of $7.7' \times 7.7'$, pixel scale of $0.4486''$pixel^{-1}. Exposures were 15 s in duration, with a total of 931 exposures taken, lasting a total of 4.6 hours. The target remained above airmass 1.25, and drifted by less than 1 pixel throughout the observations. The telescope was defocused to achieve a PSF FWHM of ~2.2$''$, in order to minimize the effect of inter- and intra-pixel variation, and prevent saturation. The observing strategy, data reduction, and light curve analysis techniques are detailed in Zhou et al. (2014a). Flat fielding is performed using a linear combination of two sets of dither frames taken before and after the observation. Aperture photometry is performed on each frame to extract the fluxes of the target and reference stars. The target light curve was corrected against the ensemble of reference stars, with weights to each reference star fitted for to minimize the out-of-transit root mean square (RMS) scatter of the target star.

All observations of HATS-11b in different filters reproduced a similar flux decrease of 12.9 mmag as seen in the discovery light curve, but with a higher precision, between 1.6 and 5 mmag per point. We note that mostly partial transits were observed. Each

TABLE 1
SUMMARY OF PHOTOMETRIC OBSERVATIONS

Instrument/Field[a]	Date(s)	# Images	Cadence[b] (sec)	Filter	Precision[c] (mmag)
HATS-11					
HS-3.1/G579	2010 Mar–2011 Aug	2229	304	r	11.5
HS-1.2/G579	2010 Mar–2011 Aug	4298	301	r	10.8
HS-3.2/G579	2010 Mar–2011 Aug	2144	304	r	11.2
HS-5.2/G579	2010 Sep–2011 Aug	2768	303	r	10.2
PEST	2013 Jun 15	138	131	R_C	4.9
Swope 1 m	2014 Jul 03	69	189	i	1.6
LCOGT 1 m+SBIG	2014 Sep 03	48	196	i	3.8
AAT+IRIS2	2014 Sep 07	778	16	K_S	3.7
LCOGT 1 m+Sinistro	2014 Sep 11	46	288	i	2.7
HATS-12					
HS-1.2/G579	2010 Mar–2011 Aug	4315	300	r	5.9
HS-3.2/G579	2010 Mar–2011 Aug	2126	303	r	6.9
HS-5.2/G579	2010 Sep–2011 Aug	2781	303	r	6.1
PEST	2013 May 24	193	130	R_C	3.4
MPG 2.2m+GROND	2013 Jul 13	279	90	g	0.8
MPG 2.2m+GROND	2013 Jul 13	271	90	r	1.9
MPG 2.2m+GROND	2013 Jul 13	273	90	i	0.7
DK 1.54m+DFOSC	2013 Oct 03	98	145	R	1.9
SWOPE 1m	2015 May 26	82	59	g	2.1

[a] For HATSouth data we list the HATSouth unit, CCD and field name from which the observations are taken. HS-1 and -2 are located at Las Campanas Observatory in Chile, HS-3 and -4 are located at the H.E.S.S. site in Namibia, and HS-5 and -6 are located at Siding Spring Observatory in Australia. Each unit has 4 ccds. Each field corresponds to one of 838 fixed pointings used to cover the full 4π celestial sphere. All data from a given HATSouth field and CCD number are reduced together, while detrending through External Parameter Decorrelation (EPD) is done independently for each unique unit+CCD+field combination.
[b] The median time between consecutive images rounded to the nearest second. Due to factors such as weather, the day–night cycle, guiding and focus corrections the cadence is only approximately uniform over short timescales.
[c] The RMS scatter of the residuals from our best fit transit model for each light curve at the cadence indicated in the table.

TABLE 2
SUMMARY OF SPECTROSCOPY OBSERVATIONS

Instrument	UT Date(s)	# Spec.	Res. $\Delta\lambda/\lambda/1000$	S/N Range[a]	$\gamma_{\rm RV}$[b] $(\rm km\,s^{-1})$	RV Precision[c] $(\rm m\,s^{-1})$
HATS-11						
ANU 2.3 m/WiFeS	2012 Sep 9	1	3	152	$\cdots$	$\cdots$
ANU 2.3 m/WiFeS	2012 Sep–2013 Mar	4	7	19–70	-53.8	4000
du Pont 2.5 m/Echelle	2013 Aug 21	1	40	40	-58.8	500
Euler 1.2 m/Coralie	2013 Aug–2014 Mar	10	60	11–17	-58.41	130
MPG 2.2 m/FEROS	2013 Apr–Sep	10	48	16–61	-58.32	42
HATS-12						
MPG 2.2 m/FEROS	2012 Aug–2013 May	12	48	57–107	-21.66	42
ANU 2.3 m/WiFeS	2012 Sep 8	1	3	257	$\cdots$	$\cdots$
Subaru 8 m/HDS+I$_2$	2012 Sep 19–22	9	60	53–86	$\cdots$	13
Subaru 8 m/HDS	2012 Sep 20	3	60	112-118	$\cdots$	$\cdots$
du Pont 2.5 m/Echelle	2013 Aug 21	1	40	58	-21.72	500

[a] S/N per resolution element near 5180 Å.
[b] For the CORALIE and FEROS observations of HATS-11, and for the FEROS observations of HATS-12, this is the zero-point RV from the best-fit orbit. For the WiFeS and du Pont Echelle it is the mean of the observations. We do not provide this quantity for HDS for which only relative RVs are measured, or for the lower resolution WiFeS observations which were only used to measure stellar atmospheric parameters.
[c] For High-precision RV observations included in the orbit determination this is the scatter in the RV residuals from the best-fit orbit (which may include astrophysical jitter), for other instruments this is either an estimate of the precision (not including jitter), or the measured standard deviation. We do not provide this quantity for low-resolution observations from the ANU 2.3 m/WiFeS or for I$_2$-free observations made with HDS, as RVs are not measured from these data.
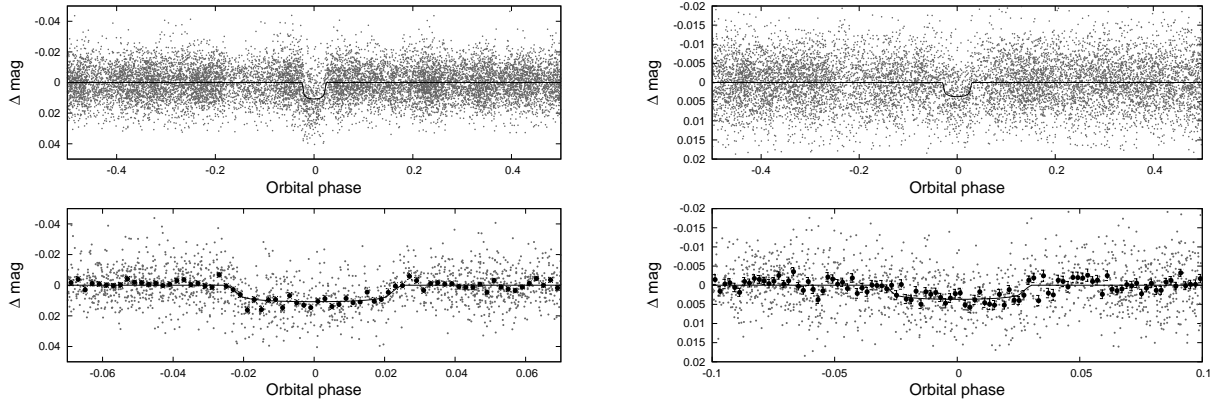
Rabus et al.

FIG. 1.— Phase-folded unbinned HATSouth light curves for HATS-11 (left) and HATS-12 (right). In each case we show two panels. The top panel shows the full light curve, while the bottom panel shows the light curve zoomed-in on the transit. The solid lines show the model fits to the light curves. The dark filled circles in the bottom panels show the light curves binned in phase with a bin size of 0.002.
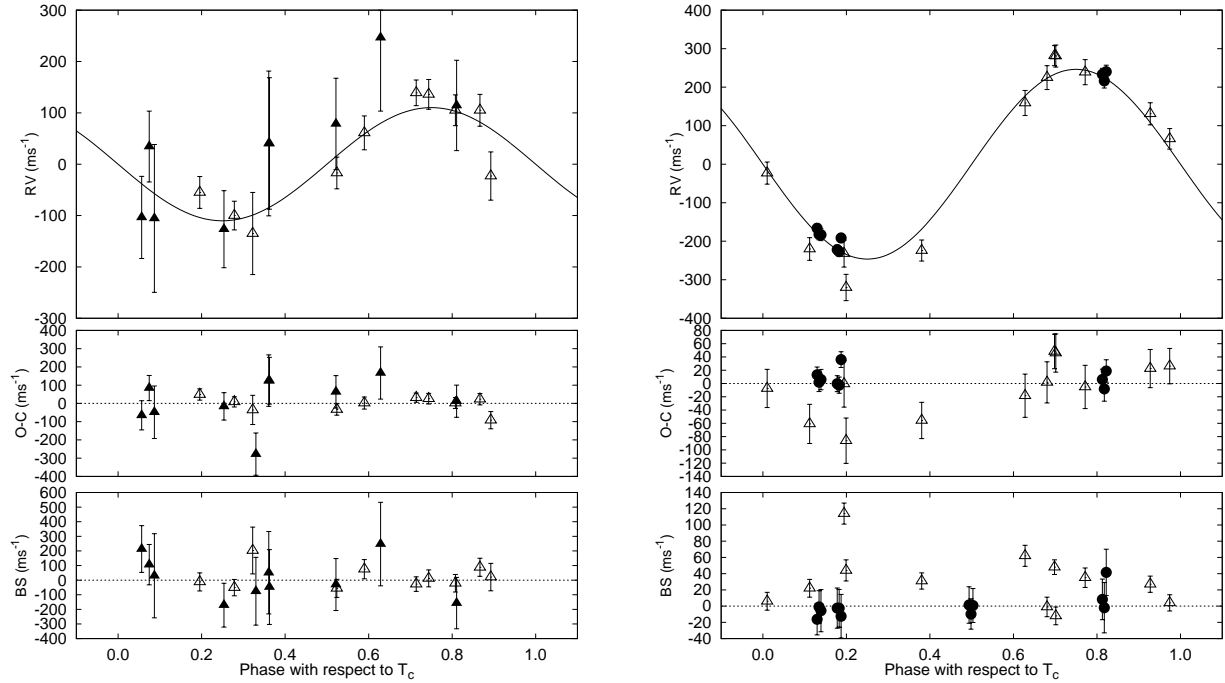

FIG. 2.— Phased high-precision RV measurements for HATS-11 (left), and HATS-12 (right) from FEROS (open triangles), CORALIE (filled triangles), and HDS (filled circles). In each case we show three panels. The top panel shows the phased measurements together with our best-fit model (see Table 5) for each system. Solid lines show the best-fit circular orbit. Zero-phase corresponds to the time of mid-transit. The center-of-mass velocity has been subtracted. The second panel shows the velocity $O-C$ residuals from the best fit. The error bars include the jitter terms listed in Table 5 added in quadrature to the formal errors for each instrument. The third panel shows the bisector spans (BS), with the median value subtracted for each instrument. Note the different vertical scales of the panels.
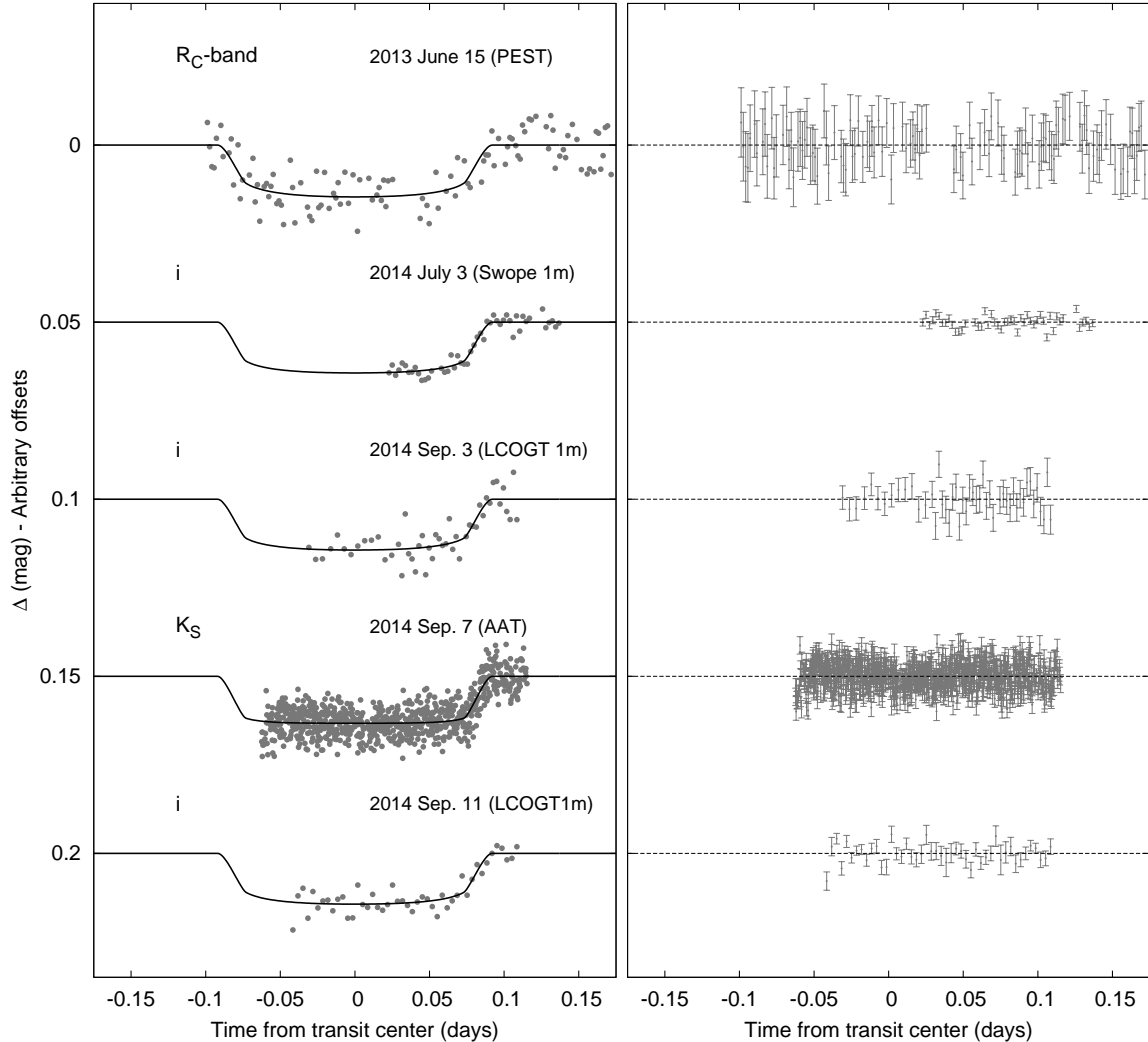
FIG. 3.— Left: Unbinned transit light curves for HATS-11. The light curves have been corrected for quadratic trends in time fitted simultaneously with the transit model. The dates of the events, filters and instruments used are indicated. Light curves following the first are displaced vertically for clarity. Our best fit from the global modeling described in Section 3.3 is shown by the solid lines. Right: residuals from the fits are displayed in the same order as the left curves. The error bars represent the photon and background shot noise, plus the readout noise.

light curve allowed us to refine and improve the uncertainties of the ephemeris, which helped us to schedule subsequent transit observations. The final ephemeris is determined through the global MCMC analysis, as explained in Section 3.3, founding them to be $T_c(\mathrm{BJD}) = 2456574.9657 \pm 0.0013$ and $P = 3.6191613 \pm 0.0000099\,days$, as well as the parameters $R_p/R_\star = 0.1076 \pm 0.0028$ and $b^2 = 0.041^{+0.060}_{-0.029}$.

HATS-12 was observed with the PEST 0.3 m, MPG 2.2 m, DK 1.54 m and the Swope 1 m telescopes. Again, their light curves were consistent with the discovery observations. For data analysis of the PEST, Swope and MPG2.2m observations we repeated our well established procedures as described in previous papers (Penev et al. (2013); Mohler-Fischer et al. (2013); Bayliss et al. (2013); Jordán et al. (2014); Zhou et al. (2014b); Hartman et al. (2015); Brahm et al. (2015); Mancini et al. (2015)). For the DK 1.54 m observation on the night 2013-10-03, we defocused the telescope. We used DFOSC, a focal reducer type camera with a

2048 × 4096 pixels E2V44-82 CCD. The CCD electronics was improved with a 32-bit analog-digital-converter (ADC), allowing for more levels than the usual 65536 available in 16-bit ADCs which are generally used for astronomical CCDs. The saturation obtained with this instrument is up to around 700000 $ADUs$ with higher readout speed (400 kpix/s) and higher gain of 0.24 $[e^-/ADU]$, and readout noise is 9.94 e^-. However, only half of the CCD is illuminated by the telescope and this part of the CCD is readout and generally referred to as full frame, while further windowing is generally possible. The field-of-view (FOV) of the illuminated part is $13.7' \times 13.7'$. This is sufficiently large to find adequate reference stars for our differential photometry. We choose a reference image and calculated the shift of all images with respect to the reference image. From the reference image we extracted the position of the stars. Following Deeg & Doyle (2013), the time series photometry was generated from these observations using optimized aperture photometry that maximizes the signal-to-noise ratio (SNR) for each star. For all images in one night we used three fixed
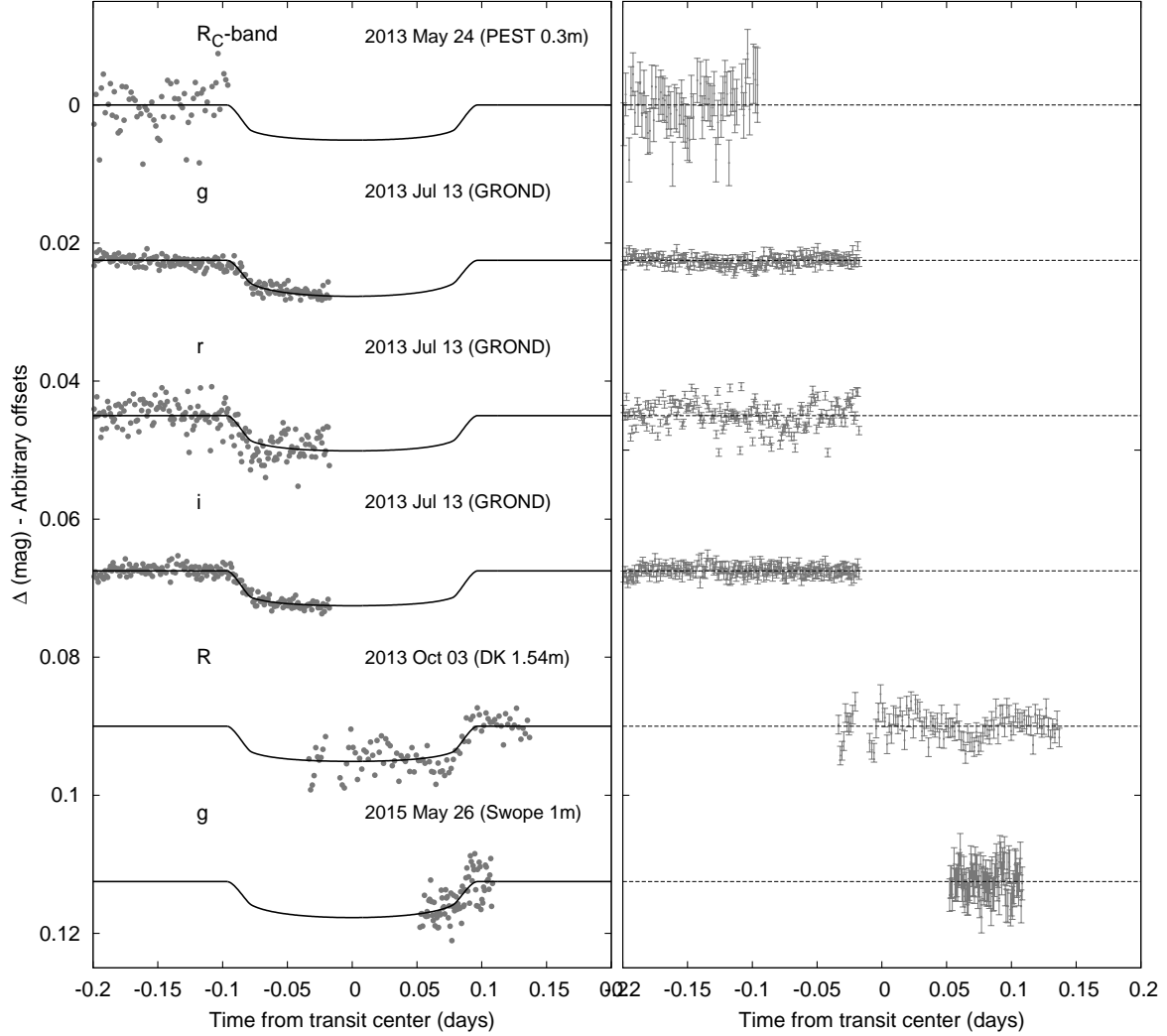
FIG. 4.— Similar to Figure 3; here we show the follow-up light curves for HATS-12. The PEST 0.3 m, observation shows a flat out-of-transit part. However, the observation helped to refine the ephemeris and the subsequent GROND observation detected the transit, see text.

apertures and choose these to be much larger than the typical point spread function in order to minimize the impact of the time-variable seeing. Depending on the telescope, for this bright object we obtained a follow-up precision between 0.7 and 3.4 mmag per point. The subsequent refinement of the transit ephemeris was especially important for HATS-12, as the first photometric follow-up observation with the PEST 0.3 m, telescope showed the flat out-of-transit part. Despite that we did not detect the transit with the our initial ephemeris, this observation was still consistent with the transit having occurred after the observation, see upper most light curve in Figure 4. We updated the ephemeris so that the following photometric observation with GROND finally revealed the transit. Again, using the procedure described in Section 3.3, the final ephemeris was determined to be $T_c(\mathrm{BJD}) = 2456798.9556 \pm 0.0012$ and $P = 3.142833 \pm 0.000011\, days$, as well as the parameters $R_p/R_\star = 0.0630 \pm 0.0022$ and $b^2 = 0.347^{+0.099}_{-0.132}$.

3. ANALYSIS

3.1. *Properties of the parent star*

In order to obtain the physical parameters of the newly discovered planets, we have to characterize their stellar hosts. We determined precise atmospheric parameters for HATS-11 and HATS-12 from the median combined FEROS spectra. The SNR of both combined spectra was ~50 per resolution element. We applied the algorithm ZASPE (Brahm et al. 2016, in prep) to both spectra which determines $T_{\rm eff}$, $\log g$, [Fe/H] and $v \sin i$ via least squares minimization against a grid of synthetic spectra in the most sensitive regions of the wavelength coverage to changes in the atmospheric parameters. ZASPE obtains reliable errors and correlations between the parameters that take into account the systematic mismatch between the data and the optimal synthetic spectra.

The $T_{\rm eff}$ and [Fe/H] values from ZASPE were combined with the stellar density ($\rho_\star$) which was obtained through our joint light curve and RV curve analysis to determine a first estimation of the stellar physical parameters (Sozzetti et al. 2007). In particular we search for the parameters of the Yonsei-Yale (Y2; Yi et al. 2001) isochrones (stellar mass, radius and age) that produce the best match with our estimated $T_{\rm eff}$, [Fe/H] and $\rho_\star$ values. Then we compute a new value for $\log g$ which is held fix in a second run of ZASPE and a subsequent comparison with the theoretical isochrones is made. The final adopted parameters for HATS-11 and HATS-12 are given in Table 4. Figure 5 shows the locations of each star on a $T_{\rm eff\star}-\rho_\star$ diagram. We found after performing the analysis just described that both stars are slightly evolved metal poor stars. HATS-11 has a mass of $1.0\pm0.06\ M_\odot$, a radius of $1.444\pm0.057\ R_\odot$ and an age of 7.7 ± 2 Gyr, while the parameters for HATS-12 are $1.489\pm0.071\ M_\odot$, $2.21\pm0.21\ R_\odot$ and an age of 2.36 ± 0.3 Gyr. Distances are determined by comparing the measured broad-band photometry listed in Table 4 to the predicted magnitudes in each filter from the isochrones. We assume a $R_V = 3.1$ extinction law from Cardelli et al. (1989) to determine the extinction.

3.2. *Excluding blend scenarios*

In order to exclude blend scenarios we carried out an analysis following Hartman et al. (2012). We attempt to model the available photometric data (including light curves and catalog broad-band photometric measurements) for each object as a blend between an eclipsing binary star system and a third star along the line of sight. The physical properties of the stars are constrained using the Padova isochrones (Girardi et al. 2000), while we also require that the brightest of the three stars in the blend have atmospheric parameters consistent with those measured with ZASPE.

For HATS-11 we find that the best-fit blend model provides a poorer fit to the data than the best-fit planet+star model, and can be rejected with 3σ confidence. Based on simulating composite spectra for the blend models that we tested, we also find that any blended eclipsing binary system that can plausibly fit the photometric data (i.e. cannot be rejected with more than 5σ confidence) would show BS variations ranging from $400\,{\rm m\,s^{-1}}$ for the model that provides the most marginal fit (i.e. at the 5σ rejection limit), to more than

$1\,{\rm km\,s^{-1}}$ for the best-fitting blend models, as well as having RV variations with $K > 200\,{\rm m\,s^{-1}}$. As the measured BS variation is $80\,{\rm m\,s^{-1}}$ for FEROS and $140\,{\rm m\,s^{-1}}$ for Coralie, and the RV semiamplitude is $112\pm15\,{\rm m\,s^{-1}}$, we conclude that HATS-11 is not a blended stellar eclipsing binary system, and that the observations favor a transiting planet system interpretation. Similarly, for HATS-12 we find that the best-fit blend model provides a poorer fit to the data than the best-fit planet+star model, and in this case can be rejected with 2σ confidence. Those blended eclipsing binary systems that cannot be rejected with more than 5σ confidence based solely on the photometry would have easily been detected as composite systems based on the FEROS and HDS spectroscopy, and would have BS variations exceeding $1\,{\rm km\,s^{-1}}$. For comparison, the BS RMS scatter is $34\,{\rm m\,s^{-1}}$ and $15\,{\rm m\,s^{-1}}$ for the FEROS and HDS observations of HATS-12, respectively. We conclude that HATS-12 is also not a blended stellar eclipsing binary system, and is instead a transiting planet system. However, both system could still be diluted transiting planet systems, which cannot be recognized by spectroscopic observations and only high angular resolution imaging can solve. If a blended stellar companion is present, diluting the light of the transiting system, then the true companion radius could be up to 60% larger than inferred.

3.3. *Global modeling of the data*

We modeled the HATSouth photometry, the follow-up photometry, and the high-precision RV measurements following Pál et al. (2008), Bakos et al. (2010) and Hartman et al. (2012). We fit Mandel & Agol (2002) transit models to the light curves, allowing for a dilution of the HATSouth transit depth as a result of blending from neighboring stars and over-correction by the trend-filtering method. For the follow-up light curves we include a quadratic trend in time in our model for each event to correct for remaining systematic errors in the photometry. We fit Keplerian orbits to the RV curves allowing the zero-point for each instrument to vary independently in the fit, and allowing for RV jitter which we also vary as a free parameter for each instrument. This jitter may be astrophysical or instrumental in nature, and simply represents excess scatter in the RV observations beyond what is expected based on formal uncertainties.

We used a Differential Evolution Markov Chain Monte Carlo procedure to explore the fitness landscape and to determine the posterior distribution of the parameters (DEMCMC; ter Braak 2006). Note that we tried fitting both fixed circular orbits and free-eccentricity models to the data, and for both systems find that the data are consistent with a circular orbit. For both systems the fixed circular orbit model has a higher Bayesian evidence so we adopt the parameters obtained assuming no eccentricity for both objects. Furthermore, we see no structure or drift within our uncertainties that could hint to any extra component in the system. We also note that for HATS-11 the scatter in the CORALIE and FEROS RV residuals is consistent with the uncertainties, so our modeling finds jitter values of 0 for both instruments. Similarly, we find that a jitter value of 0 is preferred for the HDS observations of HATS-12. For these instruments we list the 95% upper limit on the jitter in the Table 5. The resulting parameters for each system are listed in Table 5. HATS-11b

Rabus et al.

TABLE 3
Light curve data for HATS-11 and HATS-12.

Object[a]	BJD[b] (2,400,000+)	Mag[c]	σ_{Mag}	Mag(orig)[d]	Filter	Instrument
HATS-11	55780.56087	−0.01727	0.00795	⋯	r	HS
HATS-11	55762.46733	−0.01616	0.00787	⋯	r	HS
HATS-11	55802.27850	0.01253	0.00731	⋯	r	HS
HATS-11	55780.56478	0.01161	0.00824	⋯	r	HS
HATS-11	55791.42313	−0.01754	0.01052	⋯	r	HS
HATS-11	55762.47083	0.02251	0.00825	⋯	r	HS
HATS-11	55802.28203	0.00687	0.00698	⋯	r	HS
HATS-11	55273.88621	0.01511	0.00797	⋯	r	HS
HATS-11	55791.42657	−0.01138	0.01137	⋯	r	HS
HATS-11	55766.09292	0.00550	0.00705	⋯	r	HS

Note. — This table is available in a machine-readable form in the online journal. A portion is shown here for guidance regarding its form and content.
[a] Either HATS-11, or HATS-12.
[b] Barycentric Julian Date is computed directly from the UTC time without correction for leap seconds.
[c] The out-of-transit level has been subtracted. For observations made with the HATSouth instruments (identified by "HS" in the "Instrument" column) these magnitudes have been corrected for trends using the EPD and TFA procedures applied *prior* to fitting the transit model. This procedure may lead to an artificial dilution in the transit depths. For HATS-11 the transit depth is 72% and 84% that of the true depth for the G579.1 and G579.2 observations, respectively. For HATS-12 it is 100% and 78% that of the true depth for the G579.4 and G580.1 observations, respectively. For observations made with follow-up instruments (anything other than "HS" in the "Instrument" column), the magnitudes have been corrected for a quadratic trend in time fit simultaneously with the transit.
[d] Raw magnitude values without correction for the quadratic trend in time. These are only reported for the follow-up observations.
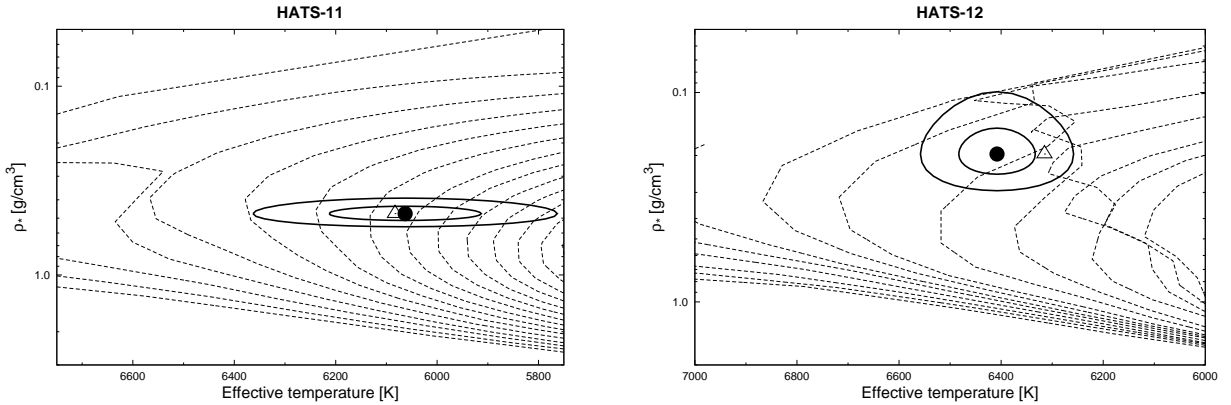

Fig. 5.— Model isochrones from Yi et al. (2001) for the measured metallicities of HATS-11 (left) and HATS-12 (right). For HATS-11 we show models for ages of 0.2 Gyr and 1.0 to 14.0 Gyr in 1.0 Gyr increments (ages increasing from left to right), while for HATS-12 we show models for ages of 0.2 Gyr, for 0.5 Gyr to 2.0 Gyr in 0.25 Gyr increments, and for 2.0 Gyr to 5.0 Gyr in 0.5 Gyr increments. The adopted values of $T_{eff\star}$ and $\rho_\star$ are shown together with their 1σ and 2σ confidence ellipsoids. The initial values of $T_{eff\star}$ and $\rho_\star$ from the first ZASPE and light curve analyses are represented with a triangle.

has a mass slightly smaller than Jupiter ($0.85\pm0.12\ M_J$) and a large radius of $1.51\pm0.078\ R_J$. It is a moderately irradiated hot Jupiter with an equilibrium temperature of 1637 ± 48 K. HATS-12b is a rather massive hot Jupiter with $2.38\pm0.11\ M_J$, $1.35\pm0.17\ R_J$ and a relatively high equilibrium temperature of 2097 ± 89 K.

TABLE 4
Stellar parameters for HATS-11 and HATS-12

Parameter	HATS-11 Value	HATS-12 Value	Source
Astrometric properties and cross-identifications			
2MASS-ID.........	2MASS 19173618-2223236	2MASS 19164857-1921212	
GSC-ID	GSC 6308-00430	GSC 6304-00396	
R.A. (J2000).......	$19^h17^m36.24s$	$19^h16^m48.72s$	2MASS
Dec. (J2000).......	$-22°23'23.7''$	$-19°21'21.2''$	2MASS
$\mu_{R.A.}$ $(mas\,yr^{-1})$	4.5 ± 1.9	6.2 ± 4.0	UCAC4
$\mu_{Dec.}$ $(mas\,yr^{-1})$	-21.5 ± 1.9	5.2 ± 2.7	UCAC4
Galactic space velocity components, LSR reference frame			
u $(km\,s^{-1})$.........	65.274	25.812	FEROS+UCAC4
v $(km\,s^{-1})$.........	88.956	37.784	FEROS+UCAC4
w $(km\,s^{-1})$	40.364	-4.115	FEROS+UCAC4
Spectroscopic properties			
$T_{eff\star}$ (K)..........	6060 ± 150	6408 ± 75	ZASPE[a]
[Fe/H]..............	-0.390 ± 0.060	-0.100 ± 0.040	ZASPE
$v \sin i$ $(km\,s^{-1})$	3.8 ± 1.0	6.57 ± 0.50	ZASPE
γ_{RV} $(km\,s^{-1})$......	-58.324 ± 0.012	-21.661 ± 0.012	FEROS[b]
Photometric properties			
B (mag)..........	14.657 ± 0.019	13.258 ± 0.043	APASS[c]
V (mag)..........	14.018 ± 0.081	12.756 ± 0.021	APASS[c]
g (mag)..........	14.268 ± 0.012	12.972 ± 0.005	APASS[c]
r (mag)..........	13.865 ± 0.039	12.654 ± 0.015	APASS[c]
i (mag)	13.506 ± 0.234	12.595 ± 0.021	APASS[c]
J (mag)	12.647 ± 0.023	11.725 ± 0.023	2MASS
H (mag)..........	12.315 ± 0.025	11.507 ± 0.024	2MASS
K_s (mag).........	12.243 ± 0.025	11.391 ± 0.023	2MASS
Derived properties			
$M_\star$ $(M_\odot)$..........	1.000 ± 0.060	1.489 ± 0.071	YY+$\rho_\star$+ZASPE [d]
$R_\star$ $(R_\odot)$..........	1.444 ± 0.057	2.21 ± 0.21	YY+$\rho_\star$+ZASPE
$\log g_\star$ (cgs)	4.118 ± 0.026	3.923 ± 0.065	YY+$\rho_\star$+ZASPE
$\rho_\star$ $(g\,cm^{-3})$........	$0.471^{+0.037}_{-0.052}$	$0.196^{+0.057}_{-0.044}$	YY+$\rho_\star$+ZASPE
$L_\star$ $(L_\odot)$...........	2.53 ± 0.39	7.3 ± 1.5	YY+$\rho_\star$+ZASPE
M_V (mag)........	3.81 ± 0.18	2.58 ± 0.22	YY+$\rho_\star$+ZASPE
M_K (mag,ESO)....	2.44 ± 0.10	1.47 ± 0.21	YY+$\rho_\star$+ZASPE
Age (Gyr)	$7.7^{+2.2}_{-1.6}$	2.36 ± 0.31	YY+$\rho_\star$+ZASPE
A_V (mag)	0.42 ± 0.15	0.228 ± 0.068	YY+$\rho_\star$+ZASPE
Distance (pc)......	906 ± 41	981 ± 94	YY+$\rho_\star$+ZASPE

[a] ZASPE = Zonal Atmospheric Stellar Parameter Estimator routine for the analysis of high-resolution spectra (Brahm et al. 2016, in preparation), applied to the FEROS spectra of HATS-11 and HATS-12. These parameters rely primarily on ZASPE, but have a small dependence also on the iterative analysis incorporating the isochrone search and global modeling of the data.
[b] The error on γ_{RV} is determined from the orbital fit to the FEROS RV measurements, and does not include the systematic uncertainty in transforming the velocities from FEROS to the IAU standard system.
[c] From APASS DR9 (Henden & Munari 2014).
[d] YY+$\rho_\star$+ZASPE = Based on the YY isochrones (Yi et al. 2001), $\rho_\star$ as a luminosity indicator, and the ZASPE results.

TABLE 5
ORBITAL AND PLANETARY PARAMETERS FOR HATS-11B AND HATS-12B

Parameter	HATS-11b Value	HATS-12b Value
Light curve parameters		
P (days)	3.6191613 ± 0.0000099	3.142833 ± 0.000011
T_c (BJD) [a]	2456574.9657 ± 0.0013	2456798.9556 ± 0.0012
T_{12} (days) [a]	0.1819 ± 0.0039	0.1899 ± 0.0031
$T_{12} = T_{34}$ (days) [a]	0.0184 ± 0.0012	0.0167 ± 0.0033
$a/R_\star$	$6.88^{+0.18}_{-0.27}$	4.67 ± 0.38
$\zeta/R_\star$ [b]	12.23 ± 0.26	11.54 ± 0.12
$R_p/R_\star$	0.1076 ± 0.0028	0.0630 ± 0.0022
b^2	$0.041^{+0.060}_{-0.029}$	$0.347^{+0.099}_{-0.132}$
$b \equiv a\cos i/R_\star$	$0.203^{+0.115}_{-0.094}$	$0.589^{+0.079}_{-0.126}$
i (deg)	88.31 ± 0.86	82.7 ± 1.9
Limb-darkening coefficients [c]		
c_1, g (linear term)	$\cdots$	0.4153
c_2, g (quadratic term)	$\cdots$	0.3276
c_1, r	0.2778	0.2509
c_2, r	0.3619	0.3789
c_1, i	0.2115	0.1762
c_2, i	0.3464	0.3706
c_1, R	0.2590	0.2295
c_2, R	0.3590	0.3783
c_1, K	-0.0081	$\cdots$
c_2, K	0.3305	$\cdots$
RV parameters		
K (m s^{-1})	112 ± 15	250.6 ± 9.4
e [d]	< 0.340	< 0.085
RV jitter FEROS (m s^{-1})	< 22.1	31 ± 16
RV jitter Coralie (m s^{-1})	< 26.3	$\cdots$
RV jitter HDS (m s^{-1})	$\cdots$	< 20.0
Planetary parameters		
M_p ($M_{\rm J}$)	0.85 ± 0.12	2.38 ± 0.11
R_p ($R_{\rm J}$)	1.510 ± 0.078	1.35 ± 0.17
$C(M_p, R_p)$ [f]	0.15	0.57
ρ_p (g cm^{-3})	$0.299^{+0.071}_{-0.050}$	$1.19^{+0.54}_{-0.32}$
$\log g_p$ (cgs)	2.959 ± 0.071	3.506 ± 0.095
a (AU)	0.04614 ± 0.00093	0.04795 ± 0.00077
$T_{\rm eq}$ (K)	1637 ± 48	2097 ± 89
Θ [g]	0.0514 ± 0.0076	$0.112^{+0.018}_{-0.012}$
$\log_{10}\langle F \rangle$ (cgs) [h]	9.211 ± 0.050	9.640 ± 0.074

NOTE. — For both objects we list the parameters assuming circular orbits. Based on Bayesian evidence, we find that such an orbit is preferred for both systems.

[a] Times are in Barycentric Julian Date calculated directly from UTC *without* correction for leap seconds. T_c: Reference epoch of mid transit that minimizes the correlation with the orbital period. T_{12}: total transit duration, time between first to last contact; $T_{12} = T_{34}$: ingress/egress time, time between first and second, or third and fourth contact.

[b] Reciprocal of the half duration of the transit used as a jump parameter in our MCMC analysis in place of $a/R_\star$. It is related to $a/R_\star$ by the expression $\zeta/R_\star = a/R_\star (2\pi(1 + e\sin\omega))/(P\sqrt{1 - b^2}\sqrt{1 - e^2})$ (Bakos et al. 2010).

[c] Values for a quadratic law, adopted from the tabulations by Claret (2004) according to the spectroscopic (ZASPE) parameters listed in Table 4.

[d] For fixed circular orbit models we list the 95% confidence upper limit on the eccentricity determined when $\sqrt{e}\cos\omega$ and $\sqrt{e}\sin\omega$ are allowed to vary in the fit.

[e] Error term, either astrophysical or instrumental in origin, added in quadrature to the formal RV errors for the listed instrument. We give the 95 % confidence upper limit when the jitter is consistent with 0 m s^{-1}.

[f] Correlation coefficient between the planetary mass M_p and radius R_p estimated from the posterior parameter distribution.

[g] The Safronov number is given by $\Theta = \frac{1}{2}(V_{\rm esc}/V_{\rm orb})^2 = (a/R_p)(M_p/M_\star)$ (see Hansen & Barman 2007).

[h] Incoming flux per unit surface area, averaged over the orbit.

4. DISCUSSION

In this paper we have presented HATS-11b and HATS-12b, two inflated gas giants orbiting a metal-poor and a subsolar metallicity star with [Fe/H] of -0.390 ± 0.060 and -0.100 ± 0.040, respectively. Globally fitting all observations we estimated precise system parameters as shown in Tables 4-5.

HATS-11b and HATS-12b are two regular hot Jupiters that present inflated radii as compared to predictions of standard theoretical models of planetary structure. However, a distinction of these transiting systems is that both of them have low metallicity stellar hosts which are evolved.

Figure 6 shows a histogram of metallicity for known hot Jupiter planet hosts. The systems' parameters were taken from the Transiting Extrasolar Planet Catalogue (TEPCat)[1]. We limited the sample to systems comparable to our discovered planets in this work by restricting it to TEPs satisfying $M_P \geq 0.47 M_J$, $0.015 \leq a \leq 0.5$ AU and around stars with 5300 K $\leq T_{eff} \leq 7200$ K (stellar spectral type G to F). The choice of $0.47\ M_J$ for the minimum mass is made based on the findings of Weiss et al. (2013) who found a break in the radius-mass relation at that mass. We also restrict the sample to have uncertainties in [Fe/H] ≤ 0.15 dex. As is now well established, giant planets are found less frequently around metal-poor stars. We note that HATS-11 is amongst the most metal poor stars detected to harbor a transiting giant planet and thus has the value of populating a sparse region of parameter space necessary to understand and validate planet formation theories. In particular, planets as massive as HATS-11b around stars with such a low metallicity can help to empirically constrain limits on the metallicity of the nebulae in the context of core-accretion theory, which can give insights of the boundaries of the formation process (Matsuo et al. 2007).

In Figure 7 we show stellar surface gravity as function of stellar radius for the same sample as in Figure 6. HATS-11 is a slightly evolved metal-poor star. Only two other systems resemble similar stellar parameters, namely HATS-9 (Brahm et al. 2015) and WASP-48 (Enoch et al. 2011), but none of them is metal-poor. Amongst the most evolved hot Jupiter hosts only two have a low metal content, namely HATS-12 and Kepler-435 (Almenara et al. 2015). No subsolar metallicity stars with similar stellar radius and surface gravity to HATS-12 have been detected so far, see Figure 7. Hence, HATS-11b and HATS-12b add new systems to the population of low-metallicity evolved stars known to host a giant planet.

Finally, we note that HATS-11 and HATS-12 were selected as targets for Kepler two-wheeled mission (K2) Campaign 7 (EPIC216414930 and EPIC218131080 respectively) under programs GO7066 and GO7067 (PI: Bakos). These targets have now been observed, and data is expected to be released on 2016 April 30. The high-precision K2 data will allow us to improve their transit parameters, especially important for HATS-12, as it shows the third shallowest ground-based transit discovery to date. Furthermore, we will have the possibility to search intensively for additional companions through the discovery of additional transits of longer period planets, see e.g. Rabus et al. (2009b), or transit timing variations (TTVs) (Rabus et al. 2009a), such as were measured in the hot Jupiter WASP-47b (Becker et al. 2015). The discovery of HATS-11b and HATS-12b thus provides a strong motivation for a combination of both ground-based detection and subsequent space-based follow-up characterization that can be fruitful and efficient.

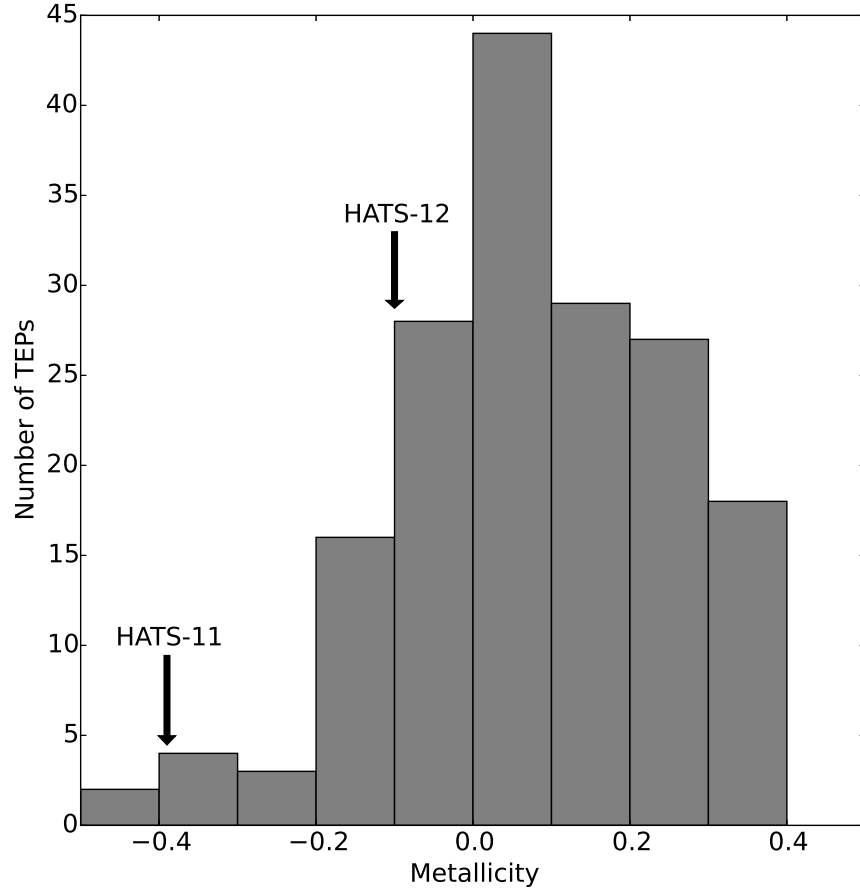[1] available at http://www.astro.keele.ac.uk/jkt/tepcat/

FIG. 6.— Histogram of stellar metallicity for 177 hot Jupiter planet hosts, see text for population parameters. HATS-12 shows sub-solar metallicity, whereas HATS-11b transits a metal-poor star where fewer systems are well characterized.
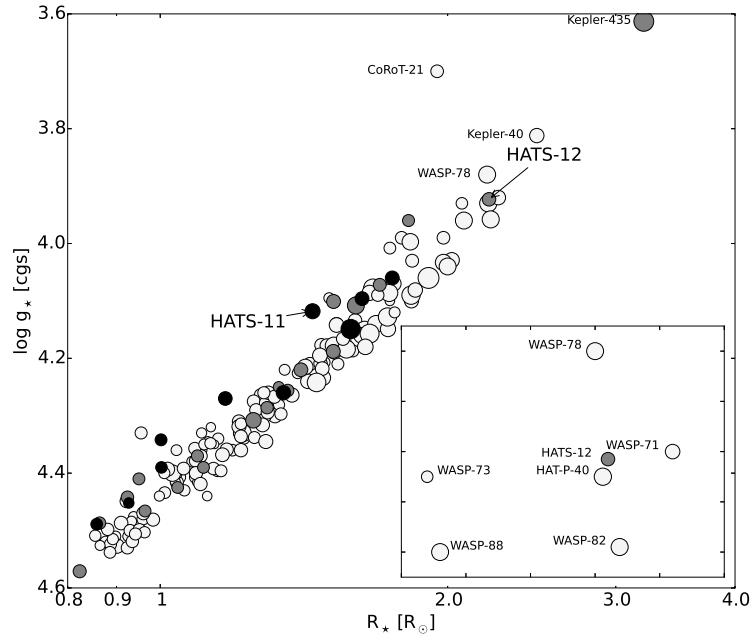

FIG. 7.— Stellar surface gravity versus stellar radius of hot Jupiter planet hosts. The host stars's metallicity is grey-color coded, grey circles show systems with $-0.2 \leq$ [Fe/H]≤ -0.1 dex and black circles [Fe/H]< -0.2. The circle's size reflect the planet's radius. Both HATS-11 and HATS-12, occupy a region where only few planet hosts are known. The inset graph in the corner shows the region around HATS-12, with planet hosting stars of similar stellar radius, we note that HATS-12 is the only low metallicity system amongst the planet hosts with similar stellar parameters.

REFERENCES

Almenara, J. M., Damiani, C., Bouchy, F., et al. 2015, A&A, 575, A71

Bakos, G. Á., Torres, G., Pál, A., et al. 2010, ApJ, 710, 1724

Bayliss, D., Zhou, G., Penev, K., et al. 2013, AJ, 146, 113

Becker, J. C., Vanderburg, A., Adams, F. C., Rappaport, S. A., & Schwengeler, H. M. 2015, ApJ, 812, L18

Brahm, R., Jordán, A., Hartman, J. D., et al. 2015, AJ, 150, 33

Buchhave, L. A., Latham, D. W., Johansen, A., et al. 2012, Nature, 486, 375

Cardelli, J. A., Clayton, G. C., & Mathis, J. S. 1989, ApJ, 345, 245

Claret, A. 2004, A&A, 428, 1001

Deeg, H. J., & Doyle, L. R. 2013, VAPHOT: Precision differential aperture photometry package, Astrophysics Source Code Library

Delrez, L., Van Grootel, V., Anderson, D. R., et al. 2014, A&A, 563, A143

Enoch, B., Anderson, D. R., Barros, S. C. C., et al. 2011, AJ, 142, 86

Everett, M. E., Howell, S. B., Silva, D. R., & Szkody, P. 2013, ApJ, 771, 107

Girardi, L., Bressan, A., Bertelli, G., & Chiosi, C. 2000, A&AS, 141, 371

Hansen, B. M. S., & Barman, T. 2007, ApJ, 671, 861

Hartman, J. D., Bakos, G. Á., Torres, G., et al. 2011, ApJ, 742, 59

Hartman, J. D., Bakos, G. Á., Béky, B., et al. 2012, AJ, 144, 139

Hartman, J. D., Bayliss, D., Brahm, R., et al. 2015, AJ, 149, 166

Henden, A., & Munari, U. 2014, Contributions of the Astronomical Observatory Skalnate Pleso, 43, 518

Johnson, J. A., Aller, K. M., Howard, A. W., & Crepp, J. R. 2010, PASP, 122, 905

Jordán, A., Brahm, R., Bakos, G. Á., et al. 2014, AJ, 148, 29

Kovács, G., Bakos, G., & Noyes, R. W. 2005, MNRAS, 356, 557

Kovács, G., Zucker, S., & Mazeh, T. 2002, A&A, 391, 369

Mancini, L., Hartman, J. D., Penev, K., et al. 2015, A&A, 580, A63

Mandel, K., & Agol, E. 2002, ApJ, 580, L171

Matsuo, T., Shibai, H., Ootsubo, T., & Tamura, M. 2007, ApJ, 662, 1282

Mohler-Fischer, M., Mancini, L., Hartman, J. D., et al. 2013, A&A, 558, A55

Pál, A., Bakos, G. Á., Torres, G., et al. 2008, ApJ, 680, 1450

Penev, K., Bakos, G. Á., Bayliss, D., et al. 2013, AJ, 145, 5

Rabus, M., Deeg, H. J., Alonso, R., Belmonte, J. A., & Almenara, J. M. 2009a, A&A, 508, 1011

Rabus, M., Alonso, R., Belmonte, J. A., et al. 2009b, A&A, 494, 391

Santos, N. C., Israelian, G., & Mayor, M. 2004, A&A, 415, 1153

Sato, B., Kambe, E., Takeda, Y., Izumiura, H., & Ando, H. 2002, PASJ, 54, 873

Sato, B., Hartman, J. D., Bakos, G. Á., et al. 2012, PASJ, 64

Schlaufman, K. C., & Laughlin, G. 2011, ApJ, 738, 177

Sozzetti, A., Torres, G., Charbonneau, D., et al. 2007, ApJ, 664, 1190

ter Braak, C. J. F. 2006, Statistics and Computing, 16, 239

Tinney, C. G., Ryder, S. D., Ellis, S. C., et al. 2004, in Society of Photo-Optical Instrumentation Engineers (SPIE) Conference Series, Vol. 5492, Ground-based Instrumentation for Astronomy, ed. A. F. M. Moorwood & M. Iye, 998–1009

Valenti, J. A., & Fischer, D. A. 2005, ApJS, 159, 141

Wang, J., & Fischer, D. A. 2015, AJ, 149, 14

Weiss, L. M., Marcy, G. W., Rowe, J. F., et al. 2013, ApJ, 768, 14

Yi, S., Demarque, P., Kim, Y.-C., et al. 2001, ApJS, 136, 417

Zhou, G., Bayliss, D. D. R., Kedziora-Chudczer, L., et al. 2014a, MNRAS, 445, 2746

Zhou, G., Bayliss, D., Penev, K., et al. 2014b, ArXiv e-prints, 1401.1582

Rabus et al.

TABLE 6
RELATIVE RADIAL VELOCITIES AND BISECTOR SPANS FOR HATS-11 AND HATS-12.

BJD (2,456,000+)	RV[a] (m s^{-1})	σ_{RV}[b] (m s^{-1})	BS (m s^{-1})	σ_{BS}[c] (m s^{-1})	Phase	Instrument
HATS-11						
400.76268	105.00	31.00	88.0	62.0	0.867	FEROS
411.71442	−23.00	47.00	21.0	94.0	0.893	FEROS
424.85662	−17.00	31.00	−56.0	62.0	0.524	FEROS
427.74603	−135.00	80.00	203.0	160.0	0.322	FEROS
488.81286	−55.00	31.00	−12.0	62.0	0.195	FEROS
490.79732	136.00	29.00	12.0	58.0	0.744	FEROS
492.73173	−100.00	28.00	−51.0	56.0	0.278	FEROS
524.50152	−103.59	80.00	213.0	160.0	0.057	Coralie
524.56679	34.41	69.00	106.0	138.0	0.075	Coralie
525.49132	−374.59	116.00	−76.0	232.0	0.330	Coralie
525.60831	40.41	128.00	−47.0	256.0	0.362	Coralie
544.52715	61.00	33.00	75.0	66.0	0.590	FEROS
548.59572	139.00	25.00	−27.0	50.0	0.714	FEROS
552.55423	105.00	30.00	−21.0	60.0	0.808	FEROS
727.88749	−126.59	75.00	−171.0	150.0	0.254	Coralie
728.85790	78.41	89.00	−30.0	178.0	0.522	Coralie
729.90376	114.41	88.00	−157.0	176.0	0.811	Coralie
730.90303	−105.59	144.00	30.0	288.0	0.087	Coralie
731.89440	40.41	141.00	51.0	282.0	0.361	Coralie
732.86378	246.41	143.00	247.0	286.0	0.629	Coralie
HATS-12						
161.57017	−232.12	29.00	114.0	13.0	0.194	FEROS
161.58536	−320.12	28.00	44.0	13.0	0.199	FEROS
169.67026	238.88	26.00	35.0	12.0	0.772	FEROS
172.52620	224.88	24.00	−1.0	12.0	0.680	FEROS
189.80413	−221.85	12.01	−2.5	24.8	0.178	HDS
189.81885	−227.15	12.14	−2.7	23.2	0.183	HDS
189.83357	−191.54	11.86	−12.5	26.9	0.187	HDS
190.79653	⋯	⋯	1.4	22.5	0.494	HDS
190.81126	⋯	⋯	−9.7	18.7	0.498	HDS
190.82599	⋯	⋯	0.8	20.9	0.503	HDS
191.79963	233.55	15.50	8.3	25.0	0.813	HDS
191.81436	216.36	18.54	−1.9	31.0	0.818	HDS
191.82908	240.25	16.91	41.6	28.5	0.822	HDS
192.79563	−166.26	11.68	−16.2	19.2	0.130	HDS
192.81036	−182.37	14.01	−0.9	19.9	0.134	HDS
192.82509	−183.11	15.32	−5.6	26.0	0.139	HDS
211.59628	−220.12	22.00	22.0	11.0	0.112	FEROS
375.86732	−224.12	19.00	31.0	10.0	0.380	FEROS
376.87669	280.88	21.00	−12.0	11.0	0.701	FEROS
377.84700	−23.12	21.00	6.0	11.0	0.010	FEROS
398.86710	281.88	17.00	48.0	9.0	0.698	FEROS
402.87705	65.88	18.00	4.0	10.0	0.974	FEROS
405.87300	130.88	21.00	27.0	10.0	0.928	FEROS
426.93117	158.88	26.00	62.0	13.0	0.628	FEROS

NOTE. — Note that for the HDS iodine-free template exposures we do not measure the RV but do measure the BS. Such template exposures can be distinguished by the missing RV value. The HDS observation of HATS-12 without a BS measurement has too low S/N in the I$_2$-free blue spectral region to pass our quality threshold for calculating accurate BS values.

[a] The zero-point of these velocities is arbitrary. An overall offset γ_{rel} fitted independently to the velocities from each instrument has been subtracted.

[b] Internal errors excluding the component of astrophysical jitter considered in Section 3.3.

[c] For FEROS and Coralie we take the BS uncertainty to be twice the RV uncertainty. For HDS the BS uncertainty is taken to be the standard error on the mean of the BS values calculated for each of the Échelle orders.